Enhanced optical nonlinearities in the near-infrared using III-nitride heterostructures coupled to metamaterials

Omri Wolf,[1,2,a)] Andrew A. Allerman,[2] Xuedan Ma,[1,2] Joel R. Wendt,[2] Alex Y. Song,[3] Eric A. Shaner,[2] and Igal Brener[1,2,a)]
[1]*Center for Integrated Nanotechnologies, Sandia National Laboratories, P.O. Box 5800, Albuquerque, New Mexico 87185, USA*
[2]*Sandia National Laboratories, P.O. Box 5800, Albuquerque, New Mexico 87185, USA*
[3]*Electrical Engineering Department, Princeton University, EQuad, Olden St, Princeton, New Jersy 08540, USA*

(Received 29 June 2015; accepted 6 October 2015; published online 15 October 2015)

We use planar metamaterial resonators to enhance by more than two orders of magnitude the near infrared second harmonic generation obtained from intersubband transitions in III-Nitride heterostructures. The improvement arises from two factors: employing an asymmetric double quantum well design and aligning the resonators' cross-polarized resonances with the intersubband transition energies. The resulting nonlinear metamaterial operates at wavelengths where single photon detection is available, and represents a different class of sources for quantum photonics related phenomena. © *2015 AIP Publishing LLC*. [http://dx.doi.org/10.1063/1.4933332]

Multi-photon processes that preserve coherence enable the exploration of quantum phenomena.[1] Materials that support such processes are usually characterized by high optical nonlinearities and the search for new types is still an active area of research, especially in light of new developments in quantum information science. In the latter context, materials with high second and third order nonlinear susceptibilities ($\chi^{(2)}$ and $\chi^{(3)}$, respectively) in the near infrared (IR) are highly desirable, especially because of the availability of single-photon detectors and on-chip processing at those wavelengths.

Large resonant nonlinear optical susceptibilities can be obtained from intersubband transitions (ISTs) in semiconductor quantum wells (QWs), by creating equally-spaced quantized electronic subbands with good dipolar overlap.[2] Strong coupling of ISTs to optical cavities has been shown at mid-IR[3–6] and THz[7] frequencies. Recently, the ISTs' nonlinearities were enhanced even further by coupling them to metamaterial (MM) resonators[8,9] and nanoantennas[10] at long to mid IR wavelengths. Since these are resonant optical nonlinearities, scaling them to shorter wavelengths (larger energies) requires increasing the energetic separation between the 3 electronic subbands used to create the resonant $\chi^{(2)}$. The conduction band offset between 'well' and 'barrier' semiconductors sets an upper bound for the largest separation between these subbands, corresponding to the second harmonic (SH) energy (2ω) in second harmonic generation (SHG). Previously used semiconductor heterostructures for mid IR optical nonlinearities have conduction band offsets of 0.38 eV (3.2 μm) for GaAs/AlGaAs and 0.51 eV (2.4 μm) for InGaAs/InAlAs.[11] Employing high conduction-band offset heterostructures for this application has also been suggested before.[12,13] In practice, the upper bound is lower because the energy of the first subband in a quantum well is always higher (by a factor inversely proportional to the square of the well's width) than the bottom of the well (a phenomenon known as "zero-point energy"). Therefore, the only way to scale these large optical nonlinearities to the near IR is to employ semiconductor materials with much larger conduction band offsets (more than 1.5 eV); III-Nitride heterostructures naturally provide such offsets.

Here, we utilize the large second order susceptibilities in the short to near IR obtained from ISTs in III-Nitride QWs, and we further enhance the efficiency by strongly coupling them to MM resonators. Our demonstration was done at a wavelength of 3.2 μm but with the proper design and growth; similar results could be obtained in the near-IR.[14] The combined QW-MM structure is very thin (about 1/20th of the free space wavelength), which means that unlike bulk nonlinear crystals, we always operate under phase matching conditions. The metamaterial resonators play the dual role of converting the polarization of the pump beam to excite ISTs (electric field must be polarized along the QW growth direction) and more significantly, increasing the evanescent optical field beneath the metal traces where the QWs are located.[8] When the metamaterial resonances are properly tuned to the ISTs, this interaction leads to strong coupling[15–17] and a greatly increased second harmonic conversion efficiency as we show below.

Figure 1(a) is a schematic of the combined structure consisting of MM resonators (i.e., nanocavities) coupled to ISTs implemented using a double QW heterostructure design. The epitaxial structure consists of 20 periods of an AlN(5 nm)/$Al_{0.19}Ga_{0.81}N$(1.4 nm)/$Al_{0.8}Ga_{0.2}N$(0.8 nm)/$Al_{0.2}Ga_{0.8}N$(1 nm) coupled-well heterostructure, where the last two layers are nominally n-type doped (Si) to 9×10^{19} cm^{-3} and 5×10^{18} cm^{-3}, respectively. The doping in the Gallium-rich 'well layer' primarily serves to increase the carrier density in the well thereby contributing to an increased nonlinear susceptibility. The doping in the Aluminum-rich 'barrier layer' contributes, after charge redistribution, to balance the strain-induced piezo-fields in the barrier. This creates a "flatter" barrier which is more effective at separating the wells, and helps to

a)Authors to whom correspondence should be addressed. Electronic addresses: owolf@sandia.gov and ibrener@sandia.gov.

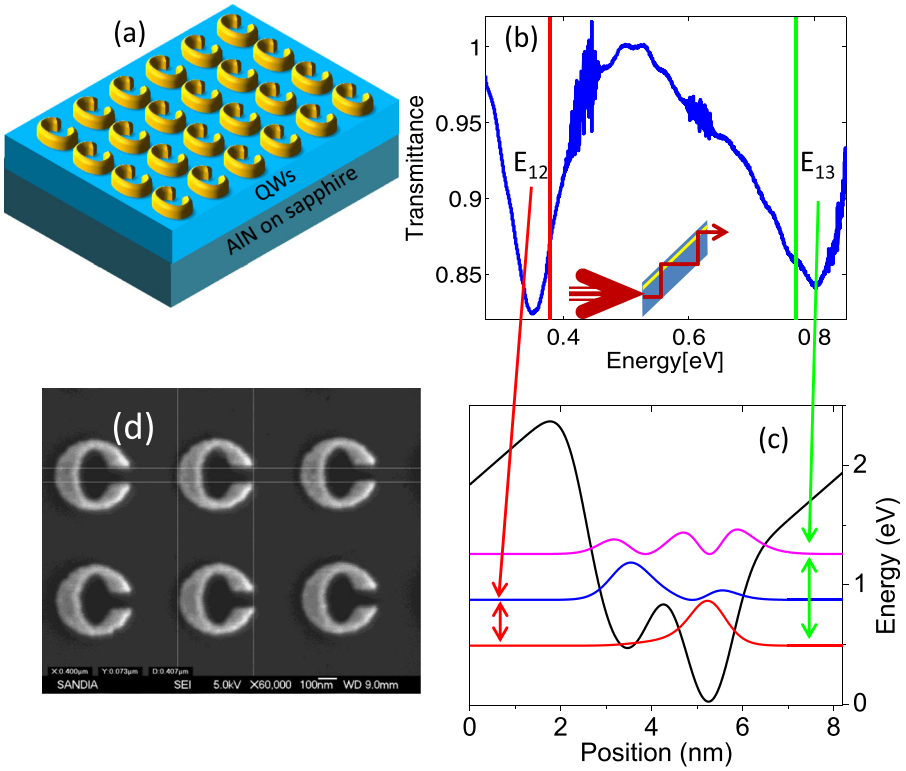

FIG. 1. (a) Schematic of the complete device showing the metamaterial resonators (Nanocavities) on top of the III-N quantum well (QW) stack. (b) Transmittance of the QWs measured in a wedge configuration (depicted by the inset). The absorption features correspond to the intersubband transitions (ISTs) marked with arrows; the vertical lines correspond to the calculated energy values according to the band structure shown in (c) Conduction band (black) and subband probability distributions derived using the effective grading interface method. (d) SEM of the resonators patterned on the sample surface.

attain the desired energetic level spacing. Metal-organic chemical vapor deposition was used to grow the coupled-well heterostructure on a previously prepared AlN epitaxial layer on sapphire. Interface sharpness was enhanced by employing a relatively low growth temperature (835 °C) to suppress interdiffusion of group-III atoms between heavily doped ($>10^{19}\,\mathrm{cm}^{-3}$) epilayers.[18] Figure 1(b) shows the measured transmittance of the QW sample measured in a wedge configuration (depicted in the inset). This spectrum was measured at TM polarization and normalized with respect to the TE polarized spectrum of the same sample. The two absorption features correspond to the 1→2 and 1→3 transitions; the vertical lines mark the transition energies (380 meV and 770 meV, respectively) calculated from the band structure presented in Figure 1(c). For this calculation, we have adopted the effective interface grading (EIG) in the structure design, which goes beyond the traditional band structure calculations in semiconductor superlattices. The existence of EIG in III-nitride QW structures is a result of three dimensional interface roughness, which we have recently shown with the help of non-equilibrium Green's functions.[19–21] EIG induces a continuous, as opposed to staggered, potential landscape in the quantum confined heterostructure and has a dramatic impact on the wave functions and energy spectra. In the band structure presented in the figure, we assume an interface roughness height of 0.4 nm. An SEM of the patterned nanocavities on the sample is shown in Figure 1(d).

Typical second order nonlinear optical materials consist of crystals that have a non-resonant $\chi^{(2)}$ that is thus fairly constant over a wide frequency range and is of the order of a few tens of pm/V.[22] Resonant systems, in general,[23] and semiconductor intersubband systems, in particular,[24] on the other hand, have been shown to have very high $\chi^{(2)}$ for a narrow spectral range where either the fundamental, the second harmonic or both frequencies of interest align with the electronic transitions. For an intersubband three-level system at near-resonant conditions, the theoretical $\chi^{(2)}$ tensor has one significant component, *zzz* (z being the growth direction). Its value at a given angular frequency ω can be approximated by[24,25]

$$\chi^{(2)}(\omega) \approx \frac{e^3}{\varepsilon_0 \hbar^2} \frac{N\mu_{12}\mu_{23}\mu_{13}}{\left(\omega - \omega_{12} - i\frac{\Gamma_{12}}{2}\right)\left(2\omega - \omega_{13} - i\frac{\Gamma_{13}}{2}\right)}, \tag{1}$$

where N is the electron density in the QWs, μ_{ij}, ω_{ij}, and Γ_{ij} are the transition dipole matrix elements, energetic differences, and dephasing rates, respectively, between level i and j. From the calculated wavefunctions (from which the probability density distribution shown in Figure 1(c) was computed), we compute the transition dipole matrix elements between the three levels ($\mu_{12} = 4.8$ Å, $\mu_{13} = 2.5$ Å, and $\mu_{23} = 7.2$ Å). We estimate the dephasing rates from the full-width-half-max of the absorption features seen in Figure 1(b) to be $\Gamma_{12} \sim 109$ THz and $\Gamma_{13} \sim 380$ THz. Our observed linewidths of 36 and 125 meV are consistent with previous reports[26,27] although these only give a lower bound to the dephasing rates. Using this, we estimate the resonant $\chi^{(2)}$ to be on the order of 0.4–3.5 nm/V for photon energies between 340–380 meV, with a maximum value occurring around 356 meV. The large uncertainty in our calculation arises from experimental ambiguities in the lifetimes of the various levels and, more significantly, the actual dopant activation percentage. These have been shown to be significantly different for "well" and "barrier" doping.[27]

Our MM nanocavities consist of gold split-ring resonators that were designed using full-wave finite-difference time-domain simulations[28] to support two dipolar

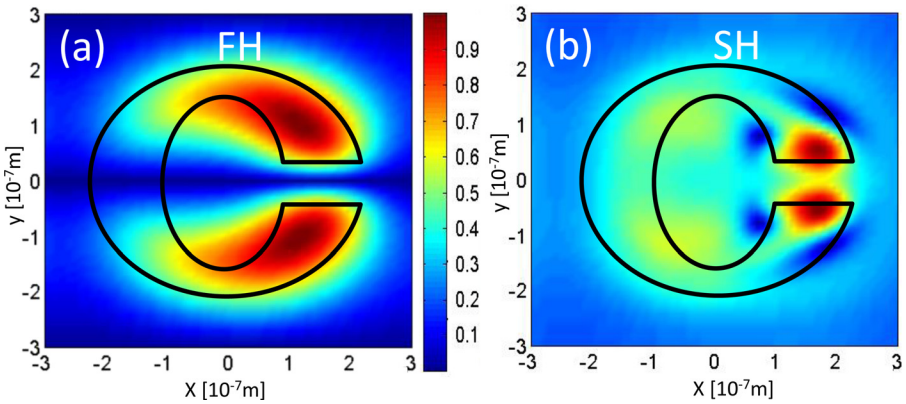

FIG. 2. (a) Normalized amplitude (with respect to the maximum) of the normal component of the electric field ($|E_z|$) in the QW stack 110 nm underneath the nanocavity, for plane wave excitation at the fundamental resonance (FR) polarized along the y axis. (b) Normalized second harmonic (SH) $|E_z|$ field generated in the QWs due to the FR excitation depicted in (a); note that the normalization factor here is 6.7×10^4 larger than in panel (a).

resonances: a *y*-polarized resonance at ~364 meV (corresponding to the fundamental frequency of interest) and an *x*-polarized resonance at twice that frequency ~729 meV. These values were chosen to match the energy at which the estimated $\chi^{(2)}$ peaks as mentioned above. The elliptical split rings are designed using a Boolean subtraction of two concentric ellipses having the following dimensions: outer ellipse: x radius = 210 nm, y radius = 170 nm, inner ellipse: x radius = 90 nm, y radius = 120 nm and a gap width of 60 nm. This design is an adaptation of a previously proven design.[9] Figure 2(a) depicts the absolute value of the simulated, out-of-plane (z-polarized), electric field in the QW region below the resonators when the system is excited at the fundamental frequency using a narrow bandwidth, plane wave pulse. Figure 2(b) depicts the out-of-plane electric field at the SH frequency for the same simulation (i.e., there is negligible input power at the monitored frequency). This field is generated by the ISTs' resonant nonlinearity. We simulate this by imparting a finite value to the *zzz* component of the $\chi^{(2)}$ tensor in the region containing the QWs. The incoming z-polarized fields enhanced by the resonators generate high SH z-polarized fields, due to the QW nonlinearity, which in turn couple efficiently back to the MM resonator (due to the higher frequency resonance) and radiate into the far field. For comparison, we "turn-off" the nonlinearity in the QW region, this results in a decrease by two-order-of-magnitudes in the field amplitudes, compared to the values depicted in Fig. 2(b), accompanied by a significant spatial redistribution (not shown). We note that because the operating principle described above relies on the evanescent near-fields around the resonator, increasing the number of QW periods beyond the evanescent field decay-length (~100 nm) does not increase the conversion efficiency. However, contrary to phase-matching limited SHG using conventional nonlinear crystals, such an increase does not reduce the efficiency either since only in the evanescent region there are significant z-polarized optical fields that can be efficiently absorbed by the ISTs.

The resonators were patterned on the sample surface in ZEP-520 resist using a JEOL 9300FS e-beam lithography system. 5 nm Ti and 100 nm Au were evaporated, and the process was completed by standard lift-off. Additional resonator arrays having resonances detuned from the predicted maximum of the ISTs' $\chi^{(2)}$ were fabricated on the same sample by scaling the resonator dimensions using scaling factors ranging from 0.85 to 1.15. Linear characterization of the different arrays using optical transmittance with a Fourier Transform IR (FTIR) spectrometer is presented in Figure 3. Each trace corresponds to the FTIR transmittance spectra for different scaling factors. The data presented in Fig. 3(a) were measured using y-polarized light (i.e., the low energy resonance is probed), while the data shown in Fig. 3(b) were obtained using x-polarized light, and the higher energy resonance is visible. Both plots show a transmission dip corresponding to the probed resonance that redshifts with increasing scaling factor, as expected. The colored regions mark the ISTs' energetic position and spectral extent (full-width-half-maximum) and show that we have a good spectral overlap between the ISTs and the cavity resonances for scaling factors 1 and 1.05.

For SHG, the device was pumped using a linearly polarized, 150 kHz repetition rate, 14 ns pulse-length optical parametric oscillator laser tuned to the fundamental frequency. A long pass filter removed unwanted wavelengths from the incident beam. A MgF_2 lens with 5 cm focal length was used to focus the incident light on the sample. The beam profile

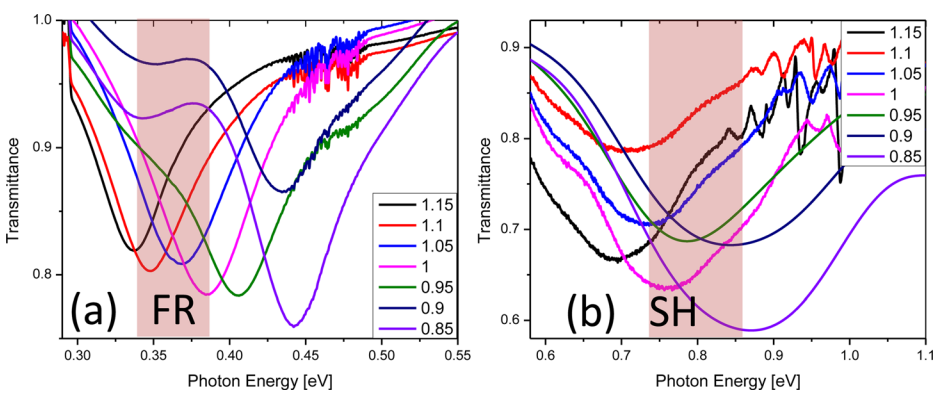

FIG. 3. (a) Transmittance spectra of arrays of metamaterial resonators for different scaling factors and for y-polarized light. The redshift of the nanocavity resonance with scaling is clearly seen. (b) Same as (a) but for x-polarized light. The colored rectangles denote the ISTs; their widths correspond to the full-width-half-maximum of the absorption features seen in Figure 1(b). The x and y polarizations align with the corresponding axes in Figure 2.

was found to be approximately Gaussian with a waist of ~50 μm. The SH signal was collected using a glass lens, and a short pass filter was used to remove the residual pump radiation. The signal was detected by a calibrated, amplified InGaAs detector and recorded using a lock-in amplifier referenced by a mechanical chopper at 250 Hz. For comparison, we used an area of the sample with no MM resonators (referred below as "QWs only"); this area was measured at Brewster incidence angle (~65°) for p-polarized light; this was done in order to minimize Fresnel reflections and maximize the amount of (out-of-plane polarized) light entering the QW heterostructure (to satisfy the ISTs' polarization selection rule[2]). Figure 4(a) presents the spectral dependence of the measured SH signal as a function of pump photon energy for the various scaling factors. For comparison, we also plot the SH signal from the QWs alone (higher pump power and renormalization was used for the "bare QWs;" all spectra were corrected for the input power's spectral variation while accounting for the quadratic relation between pump power and SH signal; detector sensitivity was measured as nearly constant at the relevant wavelength range except for the sharp cutoff seen in SH signal at around 370 meV). The resonant behavior of the "bare QW" sample confirms that the SH process originates from the ISTs rather than from any bulk nonlinearity in the constituent materials of the sample. The variation of the peak SH intensity (and spectral shape) with changing scaling factor suggests that we are not measuring the nonlinearity from the metallic resonators themselves. The overlap of the highest peak (scaling factor 1.05) with the "bare QWs" implies that the SHG indeed arises from the coupling of the metallic resonators to the ISTs. Furthermore, the presence of signal away from the peak, for the small scaling factors, is likely due to the broad $\chi^{(2)}$ response, as this heterostructure is not optimally designed.

In Figure 4(b), we plot the SH peak power as a function of pump peak power for the device (green crosses, measured at 381 meV for scaling factor 1.05) and the QWs alone (blue asterisks, also measured at 381 meV). Pump power was measured directly while the SH signal was corrected for losses from optical elements between the sample and the detector. The lines are quadratic fits ($P_{SH} = \eta P_{FR}^2$), where the conversion efficiency η is found to be 30 pW/W^2 for our device and 0.1 pW/W^2 for the "QWs only." In comparison, a recent work[29] involving SH generation from metallic resonators alone reports a conversion efficiency of 41 fW/W^2. By introducing the MM nanocavities, we improve the efficiency by more than two orders of magnitude as well as facilitate normal incidence illumination. To estimate the intersubband nonlinearity, we use a previously published method[30] where $\chi^{(2)}$ is given by

$$\chi^{(2)}(\omega) \approx \frac{c n_\omega \sqrt{2 n_{2\omega} c \varepsilon \eta_{tot}}}{\omega L}, \tag{2}$$

where c is the speed of light, ε the vacuum permittivity, n_ω and $n_{2\omega}$ are the refractive indices at the fundamental and SH frequencies, respectively, η_{tot} is the total intensity conversion efficiency, ω the fundamental angular frequency, and L the effective optical length of the nonlinear medium, when accounting for the off-normal incidence angle and refraction. We derive an experimental value for the QW $\chi^{(2)}$ of ~0.6 nm/V, which is within the range of our estimate given above. In this derivation, we compute η_{tot} inside the QWs by accounting for Fresnel reflections at the interfaces, spot-size increase due to refraction and projection of the incident/emitted radiation (the measured quantities) on the z axis (the only direction with a significant $\chi^{(2)}$ as discussed above). To verify the various assumptions used in this derivation, we performed similar measurements on a 250 μm thick GaSe crystal to arrive at a $\chi^{(2)}$ of 132 pm/V (this is slightly higher than the accepted values for GaSe ~ 112 pm/V[31]). This $\chi^{(2)}$ is much higher than what can be expected from the intrinsic $\chi^{(2)}$ of the constituent materials (~46 pm/V for AlN[32] and ~33 pm/V for GaN[33]); Following the procedure in Ref. 8, we estimate that the contribution to the SHG signal from the bulk semiconductor $\chi^{(2)}$ is nearly 2 orders of magnitude smaller. More importantly, our experimental value for the QWs' $\chi^{(2)}$ is significantly higher than previously reported for single QWs.[14] We attribute this to our design consisting of an asymmetric double well configuration (similar to designs known to increase nonlinearities in other semiconductor heterostructures[30]) rather than relying on the intrinsic piezoelectric fields for symmetry breaking as was done before.[34] Another interesting result is that since we designed the two cavity resonances to be cross polarized, we expect the SH polarization to be orthogonal to the pump polarization. To confirm this, we placed a polarizer after the sample and analyzed the emitted SH signal. The inset to Figure 4(b) depicts the SH signal as a function of the polarizer angle. Zero degrees correspond to a polarization collinear with the pump polarization. As expected, we see a clear sine squared dependence which implies that the SH signal is polarized perpendicular to the pump.

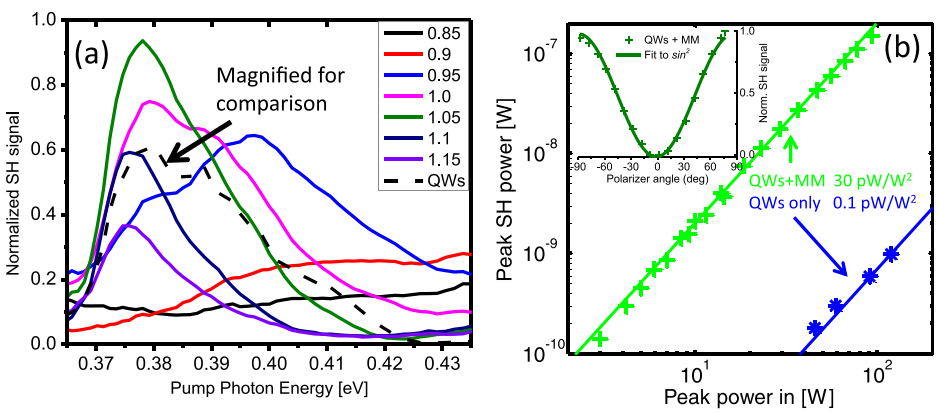

FIG. 4. (a) Spectral dependence of the SH signal for different metamaterial resonator scaling factors. The sharp signal drop around 0.37 eV arises from the detector cutoff. SH signal from the QWs alone is shown by the dashed line after magnification for comparison. (b) Peak SH power as a function of peak pumping power for the device (scaling factor 1.05) and for the QWs alone when pumping at 381 meV (3.25 μm). (inset) Normalized SH signal vs. polarizer angle, when the polarizer is placed after the sample, zero degrees is parallel to the pump polarization.

In conclusion, we have shown that using an asymmetric coupled-well design for III-N ISTs results in an increase of the nonlinear susceptibility $\chi^{(2)}$. Furthermore, by introducing metamaterial nanoresonators tuned to the ISTs' energies, an increase of more than two orders of magnitude in conversion efficiency can be achieved for a single-pass geometry with a comparable length studied here. The problem of effective homogenized susceptibilities in metamaterials (linear and nonlinear) is very complex as volumetric metamaterials are required.[35,36] This problem is particularly acute for single layer metasurfaces, and a formalism for metasurface susceptibilities has been developed only for the linear case.[37] Nevertheless, a comparison to some effective nonlinear medium that produces our measured external conversion efficiency could be made. We use a commercial nonlinear optical code[31] assuming a length of ~80 nm (the 1/e decay length of the field inside the semiconductor[15]), the correct background indices, and Fresnel reflections to calculate an effective nonlinear susceptibility of $\chi^{(2)}{}_{xyy\_eff} \sim 1.3$ nm/V, which is higher than the intrinsic $\chi^{(2)}{}_{zzz}$ of the QWs (0.6 nm/V). This work focused on SHG, but the principle should be applicable to other nonlinearities. There is much potential for increasing the QW $\chi^{(2)}$ even further, since from Equation (1) we estimate that a two-fold decrease in the dephasing rate (such values have been demonstrated[26]) combined with more precise IST energetic spacings ($\omega_{12} = \omega_{23}$) results in doubling of the effective $\chi^{(2)}$ at the resonance maximum. Additionally, increases in dopant activation (through doping profile optimizations[27]) and optimization of electron wavefunction overlaps contribute linearly to the susceptibility. Scaling to shorter wavelengths is potentially possible by growing deeper quantum wells through incorporation of Indium in these layers.

The authors thank Dr. Salvatore Campione, Sandia National Labs for fruitful discussions. This work was supported by the U.S. Department of Energy, Office of Basic Energy Sciences, Division of Materials Sciences and Engineering and performed, in part, at the Center for Integrated Nanotechnologies, an Office of Science User Facility operated for the U.S. Department of Energy (DOE) Office of Science. Sandia National Laboratories is a multiprogram laboratory managed and operated by Sandia Corporation, a wholly owned subsidiary of Lockheed Martin Corporation, for the U.S. Department of Energy's National Nuclear Security Administration under Contract No. DE-AC04- 94AL85000.

[1]M. O. Scully, *Quantum Optics* (Cambridge University Press, 2014).
[2]F. Capasso, C. Sirtori, and A. Y. Cho, IEEE J. Quantum Electron. **30**, 1313 (1994).
[3]Y. Todorov, A. M. Andrews, R. Colombelli, S. De Liberato, C. Ciuti, P. Klang, G. Strasser, and C. Sirtori, Phys. Rev. Lett. **105**, 196402 (2010).
[4]S. De Liberato, C. Ciuti, and I. Carusotto, Phys. Rev. Lett. **98**, 103602 (2007).
[5]Y. Todorov and C. Sirtori, Phys. Rev. B **85**, 045304 (2012).
[6]D. Dini, R. Köhler, A. Tredicucci, G. Biasiol, and L. Sorba, Phys. Rev. Lett. **90**, 116401 (2003).
[7]G. Scalari, C. Maissen, D. Turcinková, D. Hagenmüller, S. De Liberato, C. Ciuti, C. Reichl, D. Schuh, W. Wegscheider, M. Beck, and J. Faist, Science **335**, 1323 (2012).
[8]S. Campione, A. Benz, M. B. Sinclair, F. Capolino, and I. Brener, Appl. Phys. Lett. **104**, 131104 (2014).
[9]O. Wolf, S. Campione, A. Benz, A. P. Ravikumar, S. Liu, T. S. Luk, E. A. Kadlec, E. A. Shaner, J. F. Klem, M. B. Sinclair, and I. Brener, Nat. Commun. **6**, 7667 (2015).
[10]J. Lee, M. Tymchenko, C. Argyropoulos, P.-Y. Chen, F. Lu, F. Demmerle, G. Boehm, M.-C. Amann, A. Alù, and M. A. Belkin, Nature **511**, 65 (2014).
[11]I. Vurgaftman, J. R. Meyer, and L. R. Ram-Mohan, J. Appl. Phys. **89**, 5815 (2001).
[12]I. Morrison and M. Jaros, J. Phys. Condens. Matter **2**, 4879 (1990).
[13]F. Xie, V. R. Chaganti, A. Belyanin, A. Idziaszek, J. Kono, S. Sasa, and M. Inoue, Proc. SPIE **6485**, 64850V (2007).
[14]L. Nevou, M. Tchernycheva, F. Julien, M. Raybaut, A. Godard, E. Rosencher, F. Guillot, and E. Monroy, Appl. Phys. Lett. **89**, 151101 (2006).
[15]A. Benz, S. Campione, S. Liu, I. Montaño, J. F. Klem, A. Allerman, J. R. Wendt, M. B. Sinclair, F. Capolino, and I. Brener, Nat. Commun. **4**, 2882 (2013).
[16]S. Campione, A. Benz, J. F. Klem, M. B. Sinclair, I. Brener, and F. Capolino, Phys. Rev. B **89**, 165133 (2014).
[17]A. Benz, S. Campione, M. W. Moseley, J. J. Wierer, A. A. Allerman, J. R. Wendt, and I. Brener, ACS Photonics **1**, 906 (2014).
[18]J. J. Wierer, A. A. Allerman, and Q. Li, Appl. Phys. Lett. **97**, 051907 (2010).
[19]S.-C. Lee and A. Wacker, Phys. Rev. B **66**, 245314 (2002).
[20]J. Rammer, Rev. Mod. Phys. **63**, 781 (1991).
[21]A. Y. Song, R. Bhat, P. Bouzi, C.-E. Zah, and C. F. Gmachl, e-print arXiv:cond-mat/1507.06016v1.
[22]S. Miyata, *Nonlinear Optics: Fundamentals, Materials and Devices* (Elsevier Science, 2012).
[23]E. A. Korsunsky and M. Fleischhauer, Phys. Rev. A **66**, 033808 (2002).
[24]E. Rosencher and P. Bois, Phys. Rev. B **44**, 11315 (1991).
[25]F. Wu, W. Tian, J. Zhang, S. Wang, Q. X. Wan, J. N. Dai, Z. H. Wu, J. T. Xu, X. Y. Li, Y. Y. Fang, and C. Q. Chen, Opt. Express **22**, 14212 (2014).
[26]M. Tchernycheva, L. Nevou, L. Doyennette, F. H. Julien, E. Warde, F. Guillot, E. Monroy, E. Bellet-Amalric, T. Remmele, and M. Albrecht, Phys. Rev. B **73**, 125347 (2006).
[27]C. Edmunds, L. Tang, M. Cervantes, M. Shirazi-HD, J. Shao, A. Grier, A. Valavanis, J. D. Cooper, D. Li, G. Gardner, D. N. Zakharov, Z. Ikonić, D. Indjin, P. Harrison, M. J. Manfra, and O. Malis, Phys. Rev. B **88**, 235306 (2013).
[28]See www.lumerical.com, for more information about the software.
[29]N. Segal, S. Keren-Zur, N. Hendler, and T. Ellenbogen, Nat. Photonics **9**, 180 (2015).
[30]C. Sirtori, F. Capasso, D. L. Sivco, S. N. G. Chu, and A. Y. Cho, Appl. Phys. Lett. **59**, 2302 (1991).
[31]A. V. Smith, SNLO version 65, 2015, see www.as-photonics.com/snlo.
[32]Y. Fujii, S. Yoshida, S. Misawa, S. Maekawa, and T. Sakudo, Appl. Phys. Lett. **31**, 815 (1977).
[33]H. Y. Zhang, X. H. He, Y. H. Shih, M. Schurman, Z. C. Feng, and R. A. Stall, Appl. Phys. Lett. **69**, 2953 (1996).
[34]D. Hofstetter, E. Baumann, F. R. Giorgetta, F. Guillot, S. Leconte, and E. Monroy, Appl. Phys. Lett. **91**, 131115 (2007).
[35]D. R. Smith, D. Schurig, and J. J. Mock, Phys. Rev. E **74**, 036604 (2006).
[36]D. R. Smith and S. Schultz, Phys. Rev. B **65**, 195104 (2002).
[37]C. L. Holloway, E. F. Kuester, and A. Dienstfrey, IEEE Antennas Wirel. Propag. Lett. **10**, 1507 (2011).